Sphere entry through an oil lens floating on water

Linda B. Smolka* and Clare K. McLaughlin
Department of Mathematics, Bucknell University, Lewisburg, Pennsylvania 17837, USA

(Received 15 June 2018; published 1 April 2019)

The low-speed vertical entry of a sphere onto a two-phase fluid consisting of an oil lens floating on a water surface is examined in experiments using spheres with different radii, densities, and materials. Oil coats both the leading edge of the sphere as it penetrates the free surface of the two-phase fluid and the wall of the air-entraining cavity that forms behind the descending sphere. Spheres with lower inertia form smooth cavities whereas spheres with higher inertia develop a three-dimensional crumpled morphology along the cavity wall that we demonstrate is due to a shear-induced instability between the oil layer and surrounding water near the sphere front. Despite these different dynamics, the sphere depth at collapse, either by deep seal or rupture, scales logarithmically with sphere mass for all of the spheres examined. We also observe, for the first time to our knowledge, the following phenomena: As air evacuates the necked region of the cavity, the oil coating the cavity forms an oil filament tethering the two disjoint air cavities together before eventually breaking up into satellite drops. For the experimental conditions in this study, the oil lens at the free surface is critical to forming an air-entraining cavity; with no oil lens, only a small air pocket forms as the water completely wets the spheres either sealing the free surface or forming a quasistatic cavity.

DOI: 10.1103/PhysRevFluids.4.044001

I. INTRODUCTION

The study of sphere impact onto a free surface was begun over a century ago by Worthington and Cole in experiments using single-spark photography [1,2]. Worthington described sphere entry as either "rough," in which an air-entraining cavity forms behind a descending sphere, or "smooth," where no cavity forms at all [3]. Numerous studies have since examined the characteristics that lead to cavity formation by impacting spheres and disks as well as the shape and dynamics of cavities up to the time of collapse [3–24]. A recent review by Truscott *et al.* summarizes the current work in this field [25]. Applications of sphere and disk entry include missile entry into water, basilisk lizard locomotion on a water surface [26], and oil spill remediation [27].

Worthington found that hydrophobic spheres made by roughening, prewetting, or coating the sphere's surface with fluid produces air cavities at lower impact speeds than highly polished, hydrophilic spheres [3]. May noted that at sufficiently high entry speed, the cavities of hydrophilic and hydrophobic (handled or greased) spheres were indistinguishable [6]. Worthington suggested the shearability of a liquid coating promotes cavity formation at lower entry speed [3], which May provided evidence for by finding that spheres dipped in fluids of increasingly higher viscosity with increasingly thicker film coatings produced cavities at lower entry speeds [6]. The shearability of a liquid coating can also affect the cavity surface. In experiments of sphere entry into water, Tan *et al.* find the cavity transitions from smooth to rippled as the thickness of the oil coating a sphere is increased [23].

*lsmolka@bucknell.edu

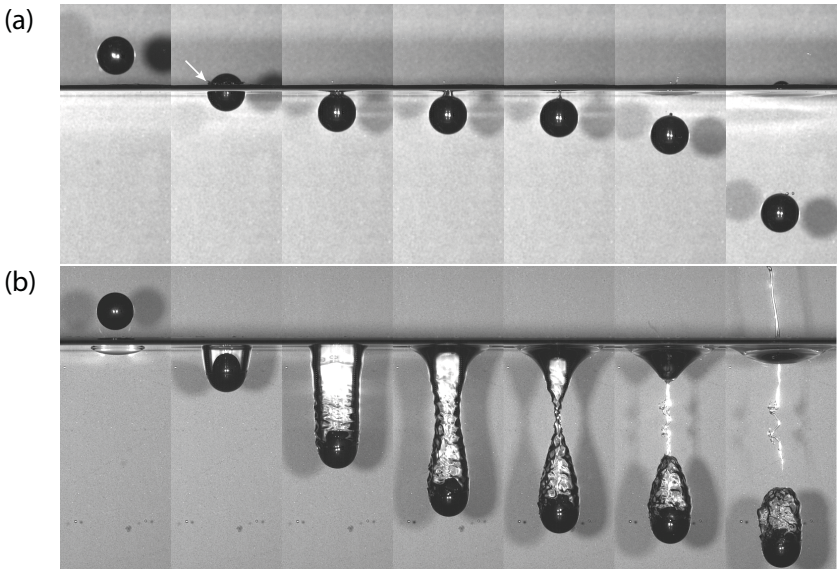

FIG. 1. Comparison of a steel sphere of radius 0.635 cm entering water at impact speed 1.0 m s^{-1} and Fr = 16.1 with (a) a clean free surface and (b) passing through an oil lens of radius 0.915 cm (left-most image). Time from impact and parameters: (a) −6.2, 5.3, 11.3, 12.0, 12.8, 17.6, 38.5 ms, Bo = 5.4, Ca = 1.4×10^{-2}, Re = 6.35×10^{3}, We = 87.2; (b) −6.0, 14.0, 36.2, 49.5, 54.1, 56.8, 63.2 ms, Bo = 7.8, Ca = 9.0×10^{-1}, Re = 139, We = 125. The arrow in panel (a) indicates the climbing water film. Supplementary movies are available in the Supplemental Material [28].

Duez *et al.* derived analytically and confirmed in experiments that the threshold impact speed U^* for a sphere to form an air-entraining cavity depends on the ratio between surface tension (σ) and viscosity (μ) and on the wettability of the sphere (represented in terms of the advancing contact angle θ_0) [11]. For sufficiently low entry speed $V_0 < U^*$, surface tension effects dominate with no air entrained [an example of a hydrophilic sphere entering water is shown in Fig. 1(a)], while for $V_0 > U^*$ viscous forces pin the solid-air-liquid contact line to the sphere, allowing an air-entraining cavity to form [11,25]. Truscott *et al.* recast this threshold impact speed in terms of a critical capillary number for cavity formation $\mathrm{Ca}^* = \mu U^*/\sigma$ [25]. The threshold values U^* and Ca^* are constant and largest for hydrophilic spheres ($U^* \approx 7.2$ m s^{-1} and $\mathrm{Ca}^* \approx 0.1$ when $\theta_0 < 90^\circ$) and decreasing functions of θ_0 for hydrophobic spheres ($\theta_0 > 90^\circ$) while superhydrophobic spheres ($\theta_0 \to 180^\circ$) form cavities at any impact speed or capillary number [11,25], thus formalizing the observations by Worthington and May that hydrophobicity promotes air entrainment by impacting spheres [3,6].

Several experimental studies have examined the evolution, shape, and dynamics of air-entraining cavities formed by hydrophobic spheres impacting water [12,14,18]. Duclaux *et al.* confirmed their theoretical predictions in experiments showing the dimensionless sphere depth at pinch-off scales as $H/R_0 \sim \sqrt{\mathrm{Fr}}$, the pinch-off time scales as $\tau_p \sim \sqrt{R_0/g}$ and the ratio of pinch-off depth to sphere depth $H_p/H \approx 1/2$ is invariant to the Froude number, where R_0 is the sphere radius, g is the acceleration due to gravity, and $\mathrm{Fr} = V_0^2/(gR_0)$ [12]. Aristoff *et al.* showed sphere deceleration after impact dramatically affects the shape and dynamics of an air-entraining cavity where a decrease in sphere density leads to decreases in the pinch-off depth, sphere depth at pinch-off, and pinch-off time [18]. While dimensionless values of these three quantities for heavier spheres followed the predicted $\sqrt{\mathrm{Fr}}$ scaling [12,18], lighter spheres that decelerated did not [18]. In generalizing Duclaux *et al.*'s model to include sphere deceleration, Aristoff *et al.* found the lowest order corrections predict the sphere depth at pinch-off to be the most sensitive to a change in sphere density and the pinch-off time the least, consistent with their experimental observations [18]. Aristoff and Bush provide an extensive experimental and theoretical study in the low-Bond-number limit, examining

inertia's influence relative to surface tension and gravity on the cavity shape and dynamics, and find as inertial effects are increased four cavity types emerge: quasistatic, shallow seal, deep seal, and surface seal [14].

While most cavities form by the pinning of the contact line to the sphere, Marston *et al.* discovered that Leidenfrost spheres, with temperature much larger than the liquid boiling point, form a vapor jacket around the sphere that prevents pinning and produces ultrasmooth cavities compared to a cold sphere [21].

Experiments of sphere impact are typically conducted with a clean free surface. However, thin immiscible fluid layers such as oil slicks, surfactants, and other contaminants on a sea surface can be expected to influence the entry of an impacting body. Here, we alter the conditions at the free surface impacted by the sphere by placing a liquid oil lens on the water surface and examine entry at low impact speed. Experiments are also conducted with a clean water surface to understand the contaminant's influence on sphere entry. We find the presence of the oil lens leads to dramatically different dynamics as shown in Fig. 1 of a sphere entering water at $V_0 = 1.0$ m s^{-1} with [Fig. 1(a)] a clean free surface where no air is entrained by the sphere and [Fig. 1(b)] an oil lens on the free surface where a long air cavity is entrained. We investigate the dynamics of this air cavity using spheres of different radii, densities, and materials.

We note that the problem considered here can be quite different than of a sphere passing through a stratified two-fluid system [23,29,30] where the sphere can get trapped above the stratified interface or entrain the upper fluid into the lower one (called tailing). Tan *et al.*, however, demonstrate that with a shallow upper layer of oil overlying water, two more entry types are observed, a rippled air-entraining cavity or a transition entry that combines tailing and rippling sans an air cavity [23]. Tan *et al.* observe in the rippled air-entraining regime that the structure, amplitude, and wavelength of the ripples increase with the oil viscosity, though the ripple structure in all experiments decreases with sphere depth as the oil entrained by the sphere depletes (see Figs. 2, 3, and 4 in Ref. [23]), that a similar rippling pattern is formed by spheres precoated with excess oil as they enter water, and that a clean sphere dropped into a tank of oil forms a smooth cavity [23]. Based on these observations, Tan *et al.* conclude the ripples along the air cavities are due to shear between the oil coating the sphere and the surrounding water [23]. Connections between our observations of the air-entraining cavity and those of Tan *et al.* will be made later in the paper.

II. EXPERIMENTAL SETUP AND PROCEDURE

The experimental setup consists of an open-top water tank, spheres ranging in diameter between $0.476 \leqslant D_0 \leqslant 2.54$ cm, and a high-speed digital-imaging camera. Before each experiment, a tank 31 cm long, 15.7 cm wide, and 20.8 cm deep was washed with an industrial cleaner, dried, and filled 13 cm deep with tap water, and either 350 or 500 μl of oleic acid (90% grade, Sigma-Aldrich) was placed on the water surface to form a liquid lens; the larger volume of oleic acid was used for the two largest spheres in our experiments. Immiscible and insoluble with water, oleic acid spreads on a water surface with spreading coefficient $S_{o/w} = 24.6$ erg cm^{-2} [31], which made it difficult to precisely control the lens size. Over all of the experiments, the lens height ranged between $0.5 \leqslant h \leqslant 1.5$ mm and the lens radius ranged between $0.86 \leqslant r \leqslant 1.48$ cm for a 350-μl lens and $1.19 \leqslant r \leqslant 1.3$ cm for a 500-μl lens. Oleic acid and water have densities $\rho_o = 0.876$ g cm^{-3} and $\rho_w = 1.0$ g cm^{-3}, surface tensions $\sigma_o = 32.5$ dyn cm^{-1} and $\sigma_w = 72.8$ dyn cm^{-1}, and dynamic viscosities $\mu_o = 40$ cP and $\mu_w = 1$ cP.

A schematic of the experimental setup is shown in Fig. 2. In all of the experiments, the oil lens was manually positioned using a pipette and approximately centered below the sphere's release point, and the sphere released a height $H_0 = 5.9$ cm above the free surface using forceps. The sphere initially passed through a 1.2-cm-thick sleeve to ensure vertical entry and entered the water at $t = 0$ with impact speed $V_0 \approx \sqrt{2gH_0} = 1.0$ m s^{-1}. Each sphere was used only once. Experiments were also conducted with only water, and to avoid contamination a separate water tank was used in these experiments. Over all of the experiments, the water temperature ranged between 19.4 and 24.7 °C.

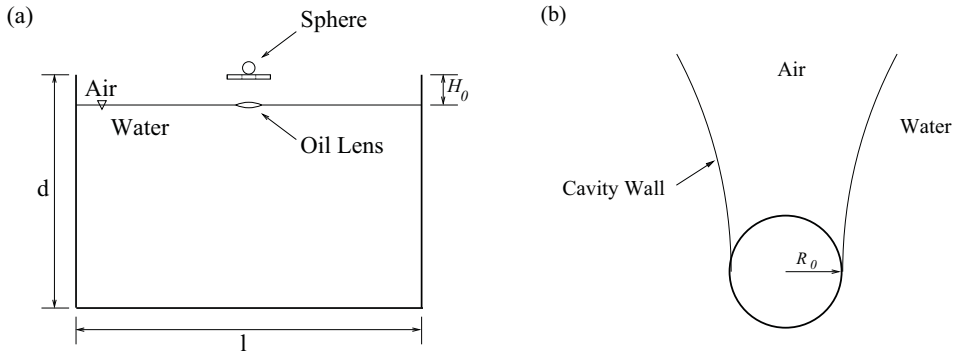

FIG. 2. (a) Schematic of experimental setup with an open-top water tank, sphere, and oil lens. The sphere is dropped from rest through a 1.2-cm-thick sleeve to ensure vertical entry. (b) After impact, a thin film of oleic acid lines the lower hemisphere and cavity wall in the oil lens experiments.

In each oil lens experiment, the sphere captures a portion of the oleic acid as it passes through the lens, forming an equilibrium pendant drop that remains attached to the top of the sphere once the sphere is at rest at the bottom of the water tank [27]. The mean value of the interfacial tension of oleic water against water in all of the experiments, $\sigma_{ow} = 12.1\,\text{dyn cm}^{-1}$, was computed by fitting these pendant drops to the Young-Laplace equation [27].

Movies of the experiments were recorded using a Vision Research Phantom v7.3 digital imaging camera at either 6000 or 9000 frames per second and analyzed using Phantom software. Illumination was obtained using two 250-W halogen lamps directed at the front of the tank with reflective screen material (Scotchlite 3M 7615) placed behind the tank. The reflective material sends back the light within an angle of 0.5° of its initial path, resulting in less scattering of light around the edges of the sphere and air cavity and a high-contrast image.

Delrin, Teflon, glass, ceramic, and steel spheres (McMaster-Carr) were examined. The densities ρ_s, equivalent to the density ratio $\mathcal{D} = \rho_s/\rho_w$, and radii of the spheres are listed in Table I along with the static contact angle at the sphere-oil-water contact line of the pendant drop attached to the sphere [27].

The relevant dimensionless groups and their range of values are listed in Table II for both the water and oil lens experiments. In the water and oil lens experiments, the capillary numbers are independent of sphere size and take on fixed values while the range of values for the Bond, Froude, Reynolds, and Weber numbers are due exclusively to changes in the sphere size. Fluid properties for water and oleic acid are used to estimate the dimensionless groups in the water and oil lens experiments, respectively. This choice allows us to develop a physical understanding of the different dynamics displayed in the water and oil lens experiments and to place into context our observations with other studies. We note that in the oil lens experiments, given the thickness of oil lining the cavity we expect the surface tension along the air cavity to be equal to the surface tension of

TABLE I. The spheres and their properties used in the experiments.

Material	ρ_s (g/cm^3) $\equiv \rho_s/\rho_w$	R_0 (cm)	Contact angle (deg)
Delrin (○)	1.35	0.238, 0.318, 0.476, 0.635, 0.953, 1.27	11.4
Teflon (□)	2.13	0.238, 0.318, 0.635, 0.953, 1.27	5.4
Glass (△)	2.41	0.318	57.4
Ceramic (◇)	3.25	0.476, 0.635	10.4
Steel (▽)	7.79	0.476, 0.635	5.0

TABLE II. Dimensionless groups and their order of magnitude values in the experiments.

Dimensionless group	Symbol	Definition	Water experiments[a]	Oil lens experiments[b]
Bond number	Bo	$\frac{\rho g R_0^2}{\sigma}$	10^{-1}–10	10^0–10
Capillary number	Ca	$\frac{\mu V_0}{\sigma}$	10^{-2}	10^{-1}
Froude number	Fr	$\frac{V_0^2}{gR_0}$	10^0–10	10^0–10
Reynolds number	Re	$\frac{\rho V_0 R_0}{\mu}$	10^3–10^4	10–10^2
Weber number[c]	We	$\frac{\rho V_0^2 R_0}{\sigma}$	10–10^2	10–10^2

[a]Computed using the values $\rho = \rho_w, \mu = \mu_w, \sigma = \sigma_w$.
[b]Computed using the values $\rho = \rho_o, \mu = \mu_o, \sigma = \sigma_o + \sigma_{ow}$.
[c]We = BoFr.

the bulk phase oil lens, $\sigma_o + \sigma_{ow}$; if, on the other hand, the oil lining was on the thickness of an insoluble monolayer, then we could expect the surface tension to be dynamic as new cavity surface is formed [32].

III. EXPERIMENTAL RESULTS

The presence of an oil lens on the free surface has a dramatic effect on sphere entry at low impact speed as illustrated in Fig. 1 for a steel sphere ($R_0 = 0.635$ cm, $V_0 = 1.0$ m s^{-1}) entering onto [Fig. 1(a)] a clean free surface and [Fig. 1(b)] an oil lens on the free surface. We investigate the conditions leading to this behavior and examine the dynamics of the air cavity.

A. Sphere entry onto water

The low Bond number ($0.76 \leqslant \text{Bo} \leqslant 21.7$) and capillary number ($\text{Ca} = 1.4 \times 10^{-2}$) in our experiments indicate surface tension controls the dynamics of sphere entry onto water as evident in the examples shown in Figs. 1(a) and 3. We see in Fig. 1(a) and in the accompanying supplementary movie [28] that as the steel sphere impacts the free surface a thin film of water climbs the sphere (indicated by the arrow in the figure), similar to other studies with hydrophilic spheres (e.g., Worthington and Cole [2], Duez *et al.* [11], Duclaux *et al.* [12]). The film's contact line continues moving up toward the sphere's apex as the sphere descends below the surface. This behavior, found for spheres with $R_0 \gtrsim 0.635$ cm, allows at most a small pocket of air to be captured behind the sphere before the surface seals as in Fig. 1(a). For smaller spheres with $R_0 \lesssim 0.635$ cm, a quasistatic impact cavity forms [14], an example of which is shown in Fig. 3. In these experiments, the contact

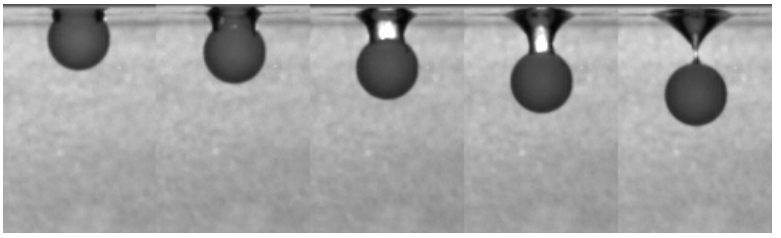

FIG. 3. A quasistatic cavity attached to a Delrin sphere of radius 0.318 cm entering water at times 5.8, 7.5, 9.2, 10.8, and 12.5 ms from impact with $V_0 = 1.0$ m s^{-1}, Bo = 1.4, $\text{Ca} = 1.4 \times 10^{-2}$, Fr = 32.1, $\text{Re} = 3.18 \times 10^3$, and We = 43.7. The quasistatic cavity shown in panel 5 can be compared to the air cavity in the corresponding oil lens experiment shown in Fig. 4(c).

line does not climb the sphere above the free surface but it does reach the apex when the sphere is below the free surface. Pinch-off occurs at or near the sphere's apex as in the fifth panel of Fig. 3, showing the moment before the funnel of air pinches off from the Delrin sphere.

Water wets all of the spheres examined in our study with no significant amount of air entrained during entry. These results are consistent with the behavior of hydrophilic spheres entering water with impact speed and capillary number below the minimum values necessary for air-entraining cavity formation (i.e., $V_0 < U^* \approx 7.2\,\mathrm{m\,s^{-1}}$ and $\mathrm{Ca} < \mathrm{Ca}^* \approx 0.1$) [11,25].

The Bond numbers for which quasistatic cavities form in our experiments lie within the range of Aristoff and Bush's experimental and theoretical study of hydrophobic spheres [14]. We note, however, that the values of the Weber number ($32.7 \leqslant \mathrm{We} \leqslant 175$) and Froude number ($8.0 \leqslant \mathrm{Fr} \leqslant 42.9$) that we observe quasistatic cavities are larger than their experimentally observed and theoretically predicted values (see Figs. 8 and 19 in Ref. [14]). This observation is consistent with cavity formation in water occurring at lower impact speeds for hydrophobic spheres than hydrophilic ones [11] which for a fixed sphere size corresponds to a lower Weber number and Froude number in the hydrophobic case.

B. Sphere entry onto oil lens

The dynamics of sphere entry onto the two-phase fluid formed by an oil lens floating on the water surface are quite different than onto water, where now an air-entraining cavity forms behind the descending sphere as shown in Figs. 1(b) and 4. All of the spheres used in our study are displayed in Fig. 4 with sphere mass increasing left to right and top to bottom and with the letters D, T, G, C, and S denoting the material. The capillary number, $\mathrm{Ca} = 0.9$, in the oil lens experiments is larger than in the water experiments and indicates viscous forces dominate over surface tension forces, leading to the different dynamics exhibited in Fig. 1. We note that the water and oil lens experiments in Fig. 1 have the same sized steel sphere, impact speed, and Froude number.

Figure 1(b) shows that as the sphere impacts the oil lens, the contact line pins to the sphere's equator, allowing air to be entrained behind the descending sphere [illustrated in panel 2 of Fig. 1(b) and in the supplementary movies [28] to Figs. 1(b) and 13]. In the process, oleic acid coats both the lower hemisphere (shown in Fig. 5) and cavity wall [the bright outline along the cavity wall in Fig. 1(b) represents the oleic acid]. The nonwetting, hydrophobic nature of the sphere is due to the direct contact of the lower hemisphere with the oleic acid, just as May discovered that handling or greasing a hydrophilic sphere's surface renders the sphere hydrophobic [6]. The pinning of the contact line and coating of oleic acid along the lower hemisphere and cavity wall occurred in all of the oil lens experiments.

The presence of the oleic acid has the combined effect of reducing the interfacial tension and increasing the viscosity along the cavity wall compared to the water experiments. This places the capillary number in the oil lens experiments ($\mathrm{Ca} = \mu V_0/\sigma = 0.9$) well above the theoretical threshold value for any sphere, hydrophilic or hydrophobic, to form an air-entraining cavity (see Fig. 2(c) in Ref. [25]); recall hydrophilic spheres have the largest threshold value ($\mathrm{Ca}^* \approx 0.1$) [25]. The strongest evidence that the spheres are hydrophobic in the oil lens experiments is given by Duez *et al.* [11], who predict theoretically and show in experiments that hydrophobic spheres with sufficiently large θ_0 form air-entraining cavities with $V_0 \leqslant 1\,\mathrm{m\,s^{-1}}$, whereas hydrophilic spheres require $V_0 \gtrsim 7.2\,\mathrm{m\,s^{-1}}$ to form an air cavity (see Fig. 2 in Ref. [11]), which is greater than the impact speed in our experiments. Based upon these comparisons to previous studies, we find that all of the spheres are rendered hydrophobic as they pass through the oil lens and that the presence of the oil lens provides the conditions for an air-entraining cavity to form for a sphere entering at low speed.

The fourth panel of Fig. 1(b) shows that as the sphere depth increases, hydrostatic pressure acting inward causes the air cavity to form an hourglass shape which drives the cavity to collapse in a deep seal closure [14] [shown in panel 5 of Fig. 1(b)]. As air evacuates the necked region at the moment of collapse, a novel to our knowledge phenomena arises in which an oil filament forms tethering

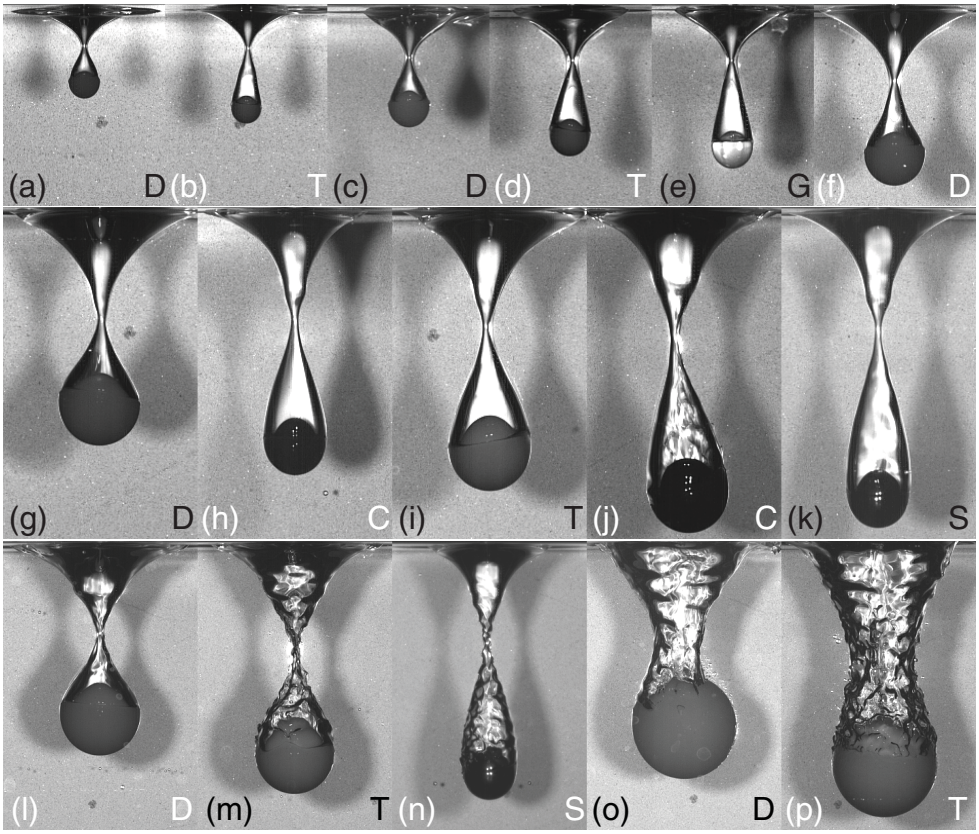

FIG. 4. Air cavity prior to deep seal pinch-off [(a)–(n)] or rupture [(o)–(p)] in oil lens experiments with sphere mass increasing left to right and top to bottom. D (Delrin), T (Teflon), G (glass), C (ceramic), and S (steel) denote sphere material. Sphere radius (frame): $R_0 = 0.238\,\text{cm}$ [(a), (b)]; $R_0 = 0.318\,\text{cm}$ [(c), (d), (e)]; $R_0 = 0.476\,\text{cm}$ [(f), (h), (k)]; $R_0 = 0.635\,\text{cm}$ [(g), (i), (j), (n)]; $R_0 = 0.953\,\text{cm}$ [(l), (m)]; $R_0 = 1.27\,\text{cm}$ [(o), (p)]. The image scale is different between rows. The air cavity for the Delrin sphere in panel (c), with $V_0 = 1.0\,\text{m}\,\text{s}^{-1}$, $\text{Bo} = 2.0$, $\text{Ca} = 9.0 \times 10^{-1}$, $\text{Fr} = 32.1$, $\text{Re} = 69.6$, and $\text{We} = 62.5$, can be compared to the quasistatic cavity in the corresponding water experiment shown in Fig. 3.

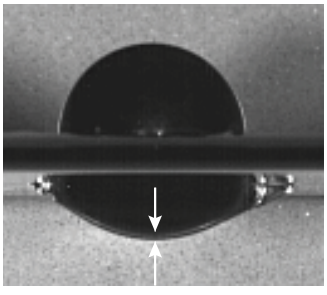

FIG. 5. A steel sphere of radius 0.635 cm passing through a lens of oleic acid that sits atop water for the experiment shown in Fig. 1(b). A thin film of oleic acid (indicated by the arrows) coats the lower hemisphere. The time from impact is 2.9 ms.

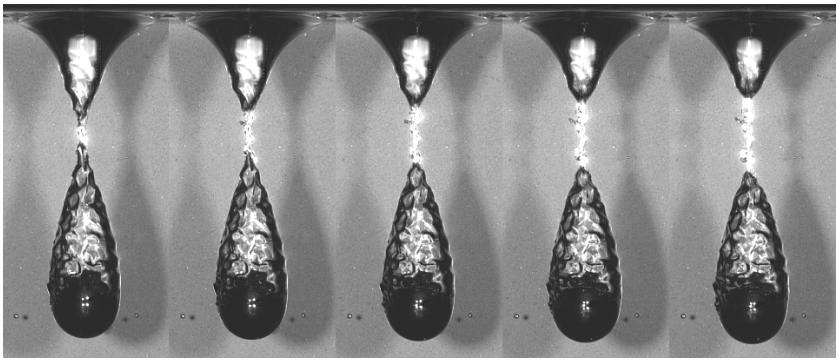

FIG. 6. Formation of oil filament after cavity collapse by deep seal closure for the experiment shown in Fig. 1(b) of a steel sphere of radius 0.635 cm. Time from impact: 54.3, 55.0, 55.7, 56.3, and 57.0 ms. Supplementary movie available online [28].

the two air cavities together as they separate from each other [shown in panel 6 of Fig. 1(b) and in greater detail in Fig. 6]; this filament is formed from the oil film coating the cavity wall.

Deep seal closure of the air cavity and formation of an oil filament connecting the two air cavities is observed when $R_0 \leqslant 0.953$ cm corresponding to the experiments shown in Figs. 4(a)–4(n). The values of the Bond number and Froude number for which deep seal closure occurs in our experiments lie within the theoretically predicted range by Aristoff and Bush [14] and Birkhoff and Isaacs [7] (see Fig. 19 in Ref. [14]). Our observations of deep seal closure are similar to observations with hydrophobic [12,18,21–23] and Leidenfrost spheres [21] with the exception that an oil filament connects the disjoint air cavities in our experiments while no such filament exists in these other studies.

For the largest spheres with $R_0 = 1.27$, the cavity completely ruptures before necking can occur. Figures 4(o)–4(p) show cavities before the onset of rupture while Fig. 7 and its accompanying movie illustrate rupture for the experiment shown in Fig. 4(p).

C. Sphere motion and cavity shape

Predictions from several theoretical and numerical studies modeling the evolution of the shape of an air cavity formed by a solid body impacting water have been shown to be in strong agreement

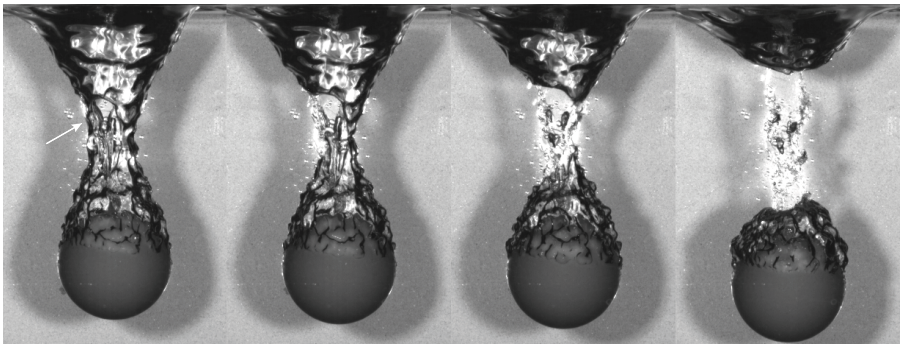

FIG. 7. Rupture of air cavity formed by a 1.27-cm-radius Teflon sphere in the oil lens experiment shown in Fig. 4(p) at times 72.5, 73.6, 74.7, and 78.0 ms from impact with lens radius 1.19 cm, Bo = 31.2, Ca = 9.0×10^{-1}, Fr = 8.0, Re = 278, We = 249. The arrow is directed toward a hole that separates the cavity into two subcavities. Supplementary movie available online [28].

with experimental observations [12,14,15,18,24]. The three-phase air-oil-water cavity in the oil lens experiments presents modeling challenges that makes it difficult to extend the analysis of these studies to the current problem. Instead, we compare predictions from these studies to data from the oil lens experiments to understand the influence the oil has on cavity formation; data from our water experiments is also presented for this same purpose.

In an analytical and experimental study, Aristoff *et al.* [18] demonstrate that sphere deceleration after impact plays a significant role in the evolution and shape of air-entraining cavities; their work generalizes the analysis of Duclaux *et al.* [12], who examined this problem under negligible deceleration. In particular, if the timescale for a sphere to decelerate to terminal speed after impact with a liquid surface of density ρ_l (Aristoff *et al.* [18])

$$\tau_s \sim \frac{R_0}{V_0}(\mathcal{D}+1)\left(1-\sqrt{\frac{\mathcal{D}-1}{\mathrm{Fr}}}\right), \tag{1}$$

with $\mathcal{D} = \rho_s/\rho_l > 1$ is less than or equal to the timescale for cavity collapse after impact (Duclaux *et al.* [12])

$$\tau_p \sim \frac{R_0}{V_0}\sqrt{\mathrm{Fr}} = \sqrt{R_0/g}, \tag{2}$$

then sphere deceleration influences the evolution of the cavity [18].

Deceleration can also be identified by examining a sphere's trajectory after impact [18,21]. Figures 8(a) and 8(b) show the trajectories of all of the spheres examined in our study from the time of impact to surface seal, pinch-off, or cavity rupture in the water and oil lens experiments, respectively. The sphere depth $z(t)$, measured to the bottom of the sphere, is normalized by the sphere diameter and the time from impact by the characteristic impact timescale D_0/V_0. The thick line in each plot represents the trajectory of a sphere traveling with impact speed V_0.

Deceleration after impact is negligible in the water experiments where the spheres travel at nearly the impact speed. Recall that little to no air is entrained in these experiments, which leads to the short time span of the data [see Fig. 8(a)]. By comparison, the time span before pinch-off or rupture in the oil lens experiments, shown in Fig. 8(b), is longer due to the entrainment of air. The sphere motion is also different where the Delrin, Teflon, and glass spheres which have the smallest density ratios ($1.35 \leqslant \mathcal{D} \leqslant 2.41$) decelerate, the ceramic spheres with moderate density ratio ($\mathcal{D} = 3.25$) travel at the impact speed, and the steel spheres with the highest density ratio ($\mathcal{D} = 7.79$) accelerate after impact. We also find that the sphere speed increases with increasing R_0 for each material.

The trajectories in the oil lens experiments are consistent with the experimental findings of Aristoff *et al.* (see Fig. 4 in Ref. [18]) who examined the impact of 1-in.-diameter hydrophobic-coated spheres onto water with density ratios that overlap with our study. In all of their experiments, air-entraining cavities form that collapse by deep seal closure with polypropylene, nylon, Delrin, and Teflon spheres ($0.86 \leqslant \mathcal{D} \leqslant 2.30$) decelerating and steel spheres ($\mathcal{D} = 7.86$) accelerating after impact. Their experiments are conducted over a range of impact speeds with $3 \leqslant \mathrm{Fr} \leqslant 100$, $10^3 \leqslant \mathrm{Re} \leqslant 10^5$, and $70 \leqslant \mathrm{We} \leqslant 2300$ [18]. The range of parameters in the oil lens experiments, $8 \leqslant \mathrm{Fr} \leqslant 43$, $10 \leqslant \mathrm{Re} \leqslant 10^2$, and $47 \leqslant \mathrm{We} \leqslant 249$, by contrast are obtained by fixing the impact speed and varying the sphere size; note that the Reynolds number is computed using the viscosity of oleic acid rather than water, resulting in lower values than Ref. [18]. The common features (sphere material, density ratio, Froude number, and Weber number) of our study with [18] provides an opportunity to compare results. We note beforehand that analogous trajectory dependence on the density ratio was observed in an experimental investigation of impact onto perfluorohexane (PP1) by cold and Leidenfrost spheres [21].

The dependence of sphere motion after impact on the density ratio influences several key features of an air-entraining cavity at pinch-off [18,21], as shown in Fig. 9. In the oil lens experiments, as the density ratio decreases, the dimensionless pinch-off depth (H_p/R_0), sphere depth at pinch-off (H/R_0), and pinch-off time ($\tau_p V_0/D_0$) decrease with this dependence most pronounced for the

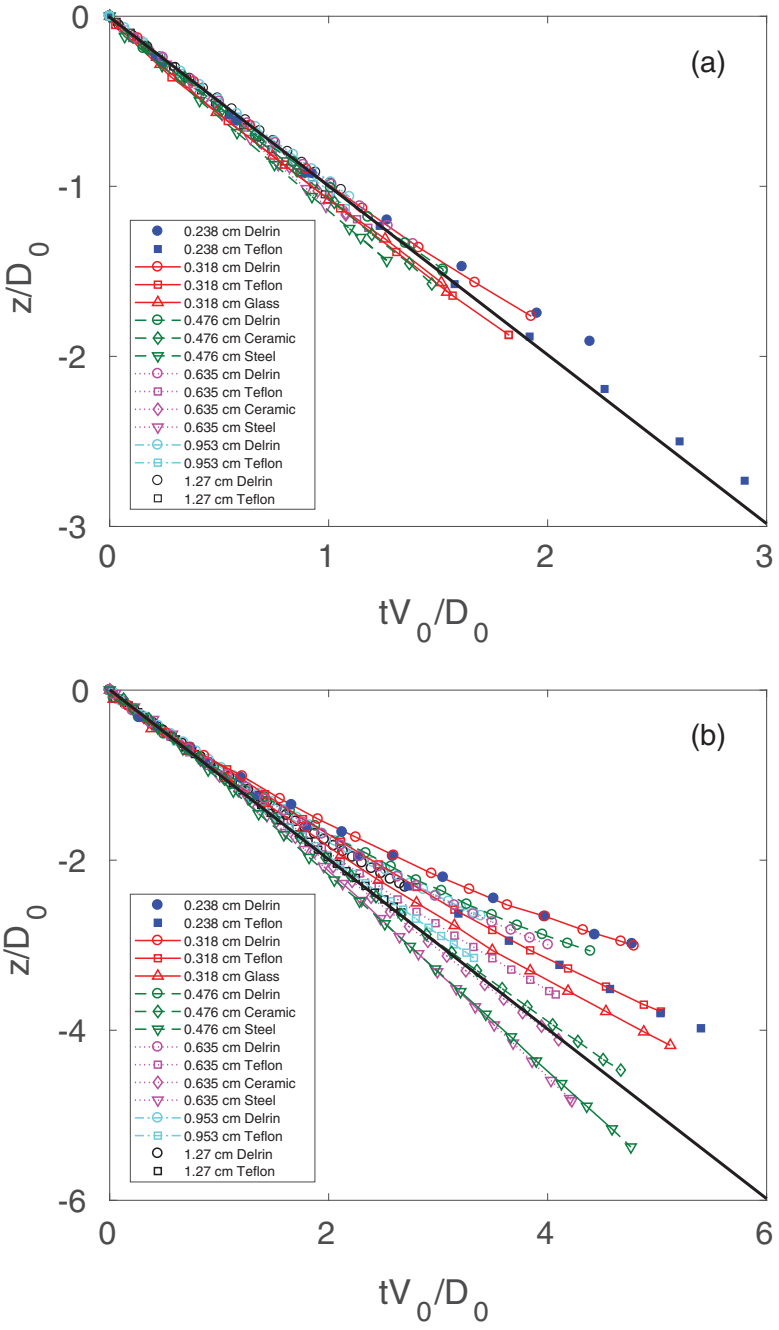

FIG. 8. Sphere trajectory after impact in the (a) water experiments and (b) oil lens experiments with sphere depth normalized by its diameter and time from impact by V_0/D_0. Symbols: ○ (Delrin, $\mathcal{D} = 1.35$), □ (Teflon, $\mathcal{D} = 2.13$), △ (glass, $\mathcal{D} = 2.41$), ◇ (ceramic, $\mathcal{D} = 3.25$), and ▽ (steel, $\mathcal{D} = 7.79$) for spheres of radii 0.238 cm (solid symbols), 0.318 cm (solid line), 0.476 cm (dashed line), 0.635 cm (dotted line), 0.953 cm (dot-dashed line), and 1.27 cm (open symbols). The thick line is the trajectory under constant speed V_0.

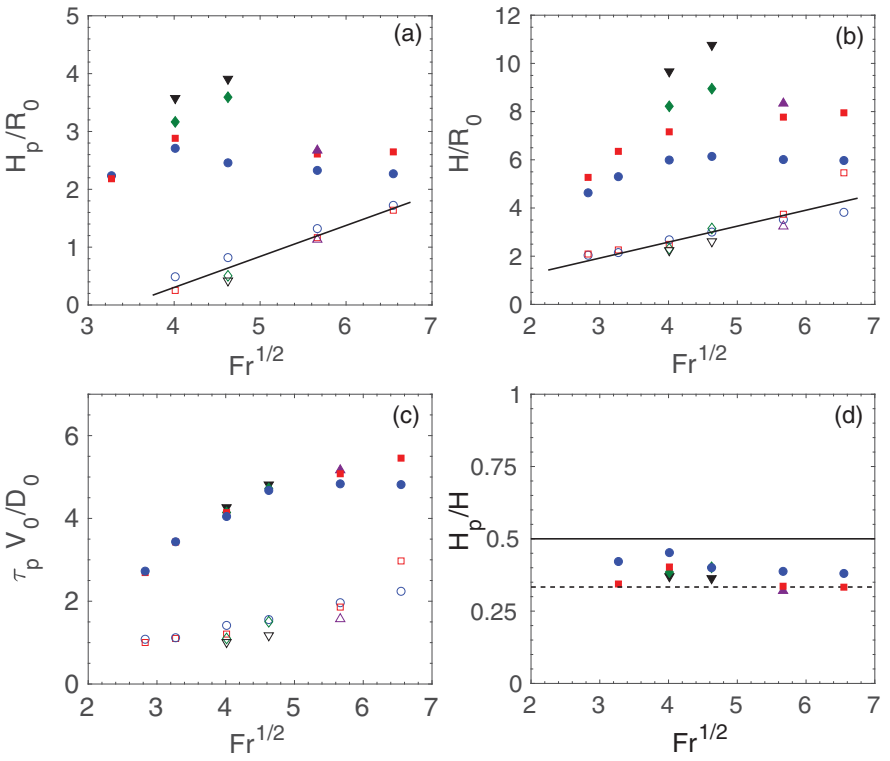

FIG. 9. Characteristics of the cavity at the time of pinch-off with dependence on $\sqrt{\text{Fr}}$ for normalized values of the (a) pinch-off depth, (b) sphere depth at pinch-off, (c) pinch-off time, and (d) ratio between the pinch-off depth and sphere depth at pinch-off. Symbols: ○ (Delrin, $\mathcal{D} = 1.35$), □ (Teflon, $\mathcal{D} = 2.13$), △ (glass, $\mathcal{D} = 2.41$), ◇ (ceramic, $\mathcal{D} = 3.25$), and ▽ (steel, $\mathcal{D} = 7.79$); water experiments (open symbols); oil lens experiments (filled symbols). Best fits of water data (solid lines): (a) $H_p/R_0 \approx 0.54\sqrt{\text{Fr}}$ and (b) $H/R_0 \approx 0.66\sqrt{\text{Fr}}$.

sphere depth at pinch-off and least for the pinch-off time. These findings are consistent with the theoretical and experimental findings for hydrophobic spheres impacting water [18] and in experimental findings for Leidenfrost spheres impacting PP1 [21].

The combined work of Duclaux *et al.* [12] and Aristoff *et al.* [18] established that dimensionless values of the pinch-off depth, sphere depth at pinch-off, and pinch-off time follow $\sqrt{\text{Fr}}$ scaling when sphere deceleration is negligible, while Aristoff *et al.* found these values scale nonlinearly with $\sqrt{\text{Fr}}$ when sphere deceleration is non-negligible. Aristoff *et al.* show that the lowest order corrections that incorporate deceleration in their model correctly predict the sphere depth at pinch-off to be the most sensitive to the density ratio and the pinch-off time the least sensitive in their experiments [18]. Comparing experimental data for the dimensionless pinch-off depth, sphere depth at pinch-off, and pinch-off time in the oil lens experiments shown in Figs. 9(a)–9(c) (filled symbols) to those of Aristoff *et al.* (see Figs. 5(a)–5(c) in Ref. [18]), we find that

(1) the data follow $\sqrt{\text{Fr}}$ scaling for spheres with negligible deceleration (i.e., ceramic and steel) in agreement with [18];

(2) the data are nonlinearly related to $\sqrt{\text{Fr}}$ for spheres with lower density ratios that decelerate after entry (i.e., Delrin, Teflon, and glass) with a similar qualitative form to [18];

(3) the dimensionless sphere depth at pinch-off H/R_0 is the most sensitive to the density ratio as found in Ref. [18];

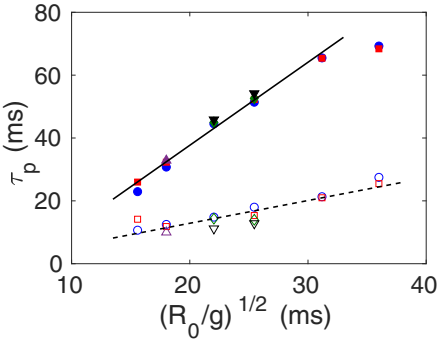

FIG. 10. Pinch-off time vs predicted scaling $\sqrt{R_0/g}$ with $\tau_p \approx 0.72\sqrt{R_0/g}$ (dashed line) and $\tau_p \approx 2.64\sqrt{R_0/g}$ (solid line). Symbols: Delrin (○); Teflon (□); glass (△); ceramic (◇); steel (▽); water experiments (open symbols); oil lens experiments (filled symbols).

(4) the dimensionless pinch-off time is the least sensitive to the density ratio with $\tau_p V_0/D_0 \sim \sqrt{\mathrm{Fr}}$ when $\sqrt{\mathrm{Fr}} \lesssim 5$. In comparison, Aristoff *et al.* observe nearly $\sqrt{\mathrm{Fr}}$ scaling over the full ranges of Froude number and density ratio used in their experiments [18].

Finally, Fig. 9(d) shows that the pinch-off depth relative to the sphere depth at pinch-off is independent of the Froude number and lies within the predicted bounds $1/3 \leqslant H_p/H \leqslant 1/2$ [12] in the oil lens experiments. There is a slight trend for this ratio to increase with decreasing density ratio similar to the experimental observations of Aristoff *et al.* (see Fig. 5(d) of Ref. [18]).

Figures 9(a)–9(c) demonstrate the effect the oil has on promoting air entrainment in this study with the pinch-off depth, sphere depth at pinch-off, and pinch-off time significantly larger than in the corresponding water experiments (open symbols). The spheres in the water experiments experience negligible deceleration which may explain the observable $\sqrt{\mathrm{Fr}}$ scaling of the pinch-off depth and sphere depth at pinch-off shown in Figs. 9(a) and 9(b) even though at most a small amount of air is entrained by these spheres.

It has been widely verified in experiments that the time for cavity collapse follows the predicted $\sqrt{R_0/g}$ scaling [Eq. (2)] introduced by Duclaux *et al.* [12]. Prefactors of 2.06, 1.73, and 2.09 were found, respectively, for hydrophobic spheres impacting water [12], spinning spheres entering water [17], and Leidenfrost steel spheres impacting PP1 [21]. Prefactors ranging between 2.16 and 2.19 were reported for spheres impacting a two-layer system composed of viscous oil overlying water [23]. And Glasheen and McMahon report a prefactor of 2.285 for cavities formed by circular disks impacting water [9].

The pinch-off time in the water and oil lens experiments also follow the $\sqrt{R_0/g}$ scaling, as shown in Fig. 10, with a prefactor of 2.64 in the oil lens experiments that collapse by deep seal closure and 0.72 in the water experiments. Cavities of the largest spheres with $R_0 = 1.27$ cm rupture before collapse in the oil lens experiments and do not follow this scaling, as seen in the figure. The collapse of the data in the oil lens experiments further illustrates that the pinch-off time is nearly invariant to the density ratio, consistent with the experimental observations of Truscott and Techet [17]. The relatively small prefactor in the water experiments is due to the hydrophilic nature of the spheres impacting water where at most a quasistatic cavity forms and the larger prefactor in the oil lens experiments is attributed to the spheres having a nonconstant speed after impact [shown in Fig. 8(b)].

In a final observation, we find that the sphere depth at pinch-off in the oil lens experiments universally scales logarithmically with the sphere mass as shown in Fig. 11. This behavior holds for cavities that collapse by deep seal or rupture and for spheres that experience either negligible or non-negligible deceleration after impact. Although a physical understanding of this scaling is not yet understood, we plan to examine this phenomena in a future theoretical study. We note that

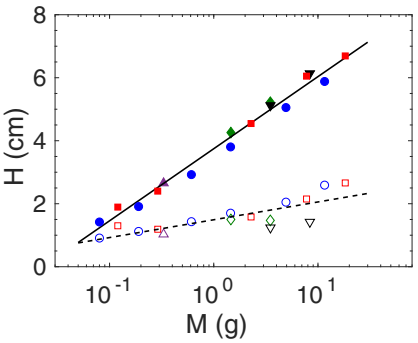

FIG. 11. Sphere depth at pinch-off vs sphere mass with $H \approx 0.57\log(M)$ (dashed line) and $H \approx 2.29\log(M)$ (solid line). Symbols: Delrin (○); Teflon (□); glass (△); ceramic (◇); steel (▽); water experiments (open symbols); oil lens experiments (filled symbols).

this same scaling does not hold in the water experiments where the resolution bars for the data are roughly the symbol size and where little to no air was entrained by the spheres.

The behaviors exhibited in the oil lens experiments by the spheres after impact and the cavities at pinch-off are remarkably similar to those displayed by hydrophobic spheres entering water [12,18]. For the low impact speed examined within our study, the presence of the oil lens is critical to forming an air-entraining cavity as the initially hydrophilic spheres are rendered hydrophobic as they come into contact with the oil lens. The behavior exhibited by the cavities at pinch-off, illustrated in Figs. 9(a)–9(c) and 10, provides further evidence that hydrophobicity promotes air entrainment, leading to the different dynamics displayed in the oil lens and water experiments.

D. Cavity dynamics in the oil lens experiments

Figure 4 shows that the air cavities formed in the oil lens experiments transition from smooth [Figs. 4(a)–4(i)] to slightly rippled [Figs. 4(j)–4(l)] to displaying three-dimensional perturbations with a crumpled morphology [Figs. 4(m)–4(p)] as the sphere mass increases. We highlight the distinctive features and dynamics of smooth and perturbed cavities and compare these observations to other related studies.

In our experiments, spheres with radii smaller than the oil lens that decelerate after entry form smooth air-entraining cavities. The accompanying oil filament that forms after deep seal closure is also smooth. For example, Figs. 4(e) and 12 show the same 0.318-cm-radius glass sphere before and after cavity pinch-off, respectively. In this experiment, the contact line remains azimuthally unperturbed as the air-entraining cavity forms. After deep seal closure, the smooth oil filament tapers down to form a thinner secondary filament (third panel of Fig. 12), pinches off from the lower and upper air cavities, and the free filament retracts to form satellite drops under the end-pinching mechanism [33] (shown in the supplementary movie [28] to Fig. 12). We also observe that after pinch-off air bubbles are released from the lower air cavity (fifth panel of Fig. 12).

Some of these observations can vary between experiments. For example, the tapering of the oil filament to a secondary filament is unique to the glass sphere and an oil filament can retract to form one satellite drop or break up into multiple drops by a capillary-wave instability, end pinching, or a combination of the two. However, in all of the experiments that form a smooth cavity, the contact line remains azimuthally unperturbed before deep seal closure.

Studies on sphere entry have reported on a variety of disturbances that develop along air-entraining cavities prior to pinch-off, including vertical striations and ripple-like structures [4,14,21,23]. In a study of sphere entry onto water, Tan *et al.* conjecture the shearability of oil coating a sphere affects the cavity surface with the cavities in their experiments transitioning from a smooth to rippled surface as the thickness of the oil coating was increased [23]. In

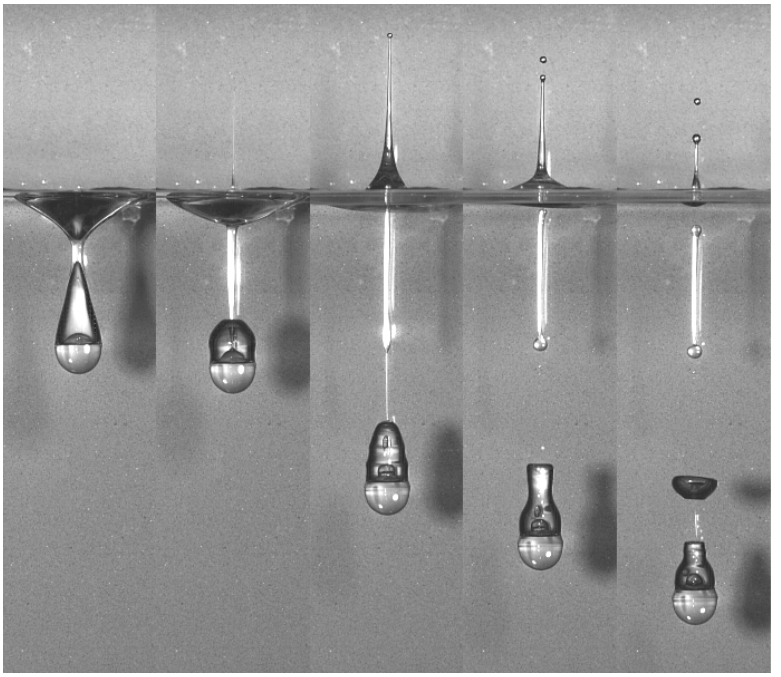

FIG. 12. Dynamics after pinch-off of an air cavity formed by a 0.318-cm-radius glass sphere in the oil lens experiment shown in Fig. 4(e) at times 33.3, 38.0, 69.6, 85.1, and 101.2 ms from impact with lens radius 0.965 cm, Bo = 2.0, Ca = 9.0×10^{-1}, Fr = 32.1, Re = 69.6, We = 62.5. Supplementary movie available online [28].

our experiments, the transition from smooth to perturbed cavities is due to a shear-induced instability triggered along the lower hemisphere which we find for spheres of sufficiently high mass that have negligible deceleration after impact or who have nearly equal radius as the oil lens. Although the transition to a perturbed surface in our experiments is caused by increased shearability of the oil coating, the effect is not associated with increases in the oil thickness as in Tan *et al.* [23].

Figures 13 and 14 show examples that track the evolution of this instability for the steel sphere in Fig. 1(b) and the Teflon sphere in Fig. 4(m). The instability begins with shear-induced perturbations developing below the contact line between the surrounding water and the oil lining the sphere front (this is easier to see in Fig. 14 and in the supplementary movies [28] to Figs. 13 and 14). These perturbations impose temporal azimuthal disturbances to the contact line that generate nascent interfacial waves along the initially smooth cavity (colored arrows track examples of individual perturbations in Figs. 13 and 14). The interfacial waves along the air cavity evolve into a highly irregular crumpled morphology as hydrostatic pressure forces the cavities to contract into an hourglass shape. While we can only track disturbances along the profiles of the spheres, perturbations develop along the entire periphery of the sphere, e.g., given the form of the contact line along the cavity front in Fig. 14. Movies are particularly useful to witness this instability, and we direct the reader to the supplementary movies [28] provided to Figs. 7, 13, 14, and 15. The behavior exhibited in these experiments is different than those with smooth air-entraining cavities shown earlier where the shear-induced instability between the oil and water is absent and the contact line remains azimuthally unperturbed.

In our experiments, we find the amplitude and steepness of the interfacial waves generated at the contact line and the number of oil drops shed by the interfacial waves increase with the sphere

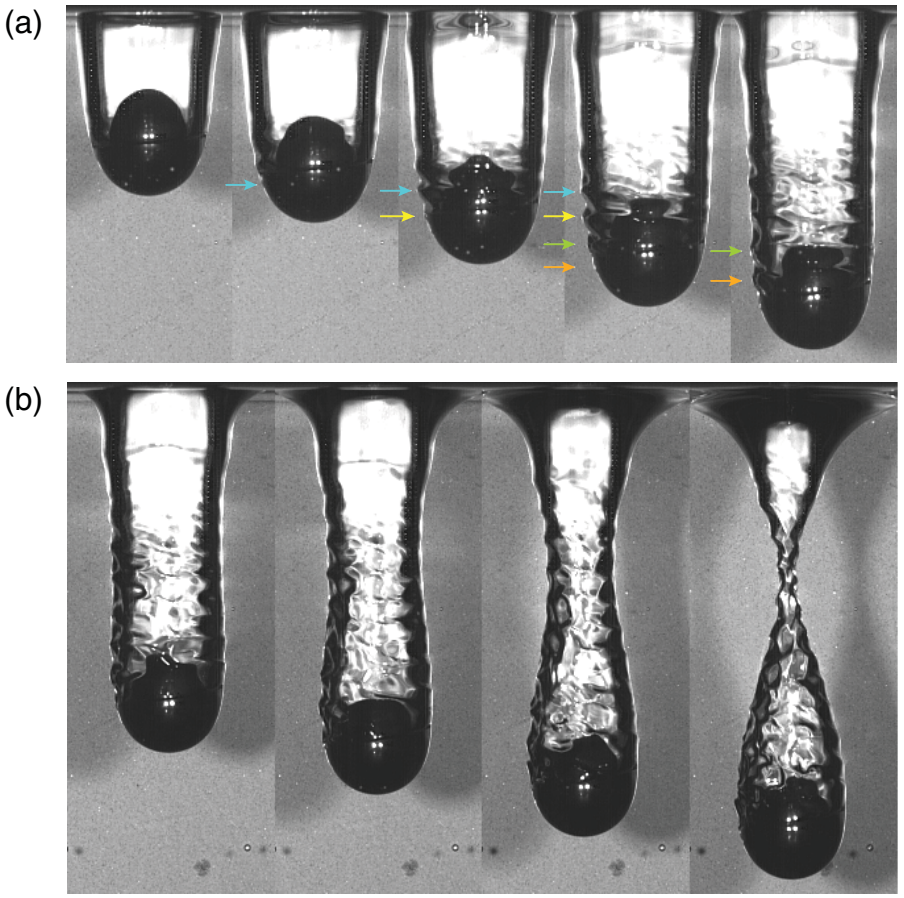

FIG. 13. (a) Shear-induced perturbations that develop along the lower hemisphere generate interfacial waves at the contact line that perturb the cavity wall (colored arrows track a few examples), and (b) then take on a three-dimensional form as the cavity contracts under hydrostatic pressure corresponding to the oil lens experiment shown in Fig. 1(b) with a 0.635-cm-radius steel sphere. Time from impact: (a) 20.0, 22.9, 27.3, 31.7, 36.1 and (b) 40.6, 45.1, 49.5, 53.9 ms. Supplementary movie available online [28].

size, which may indicate the magnitude of shear in the flow. For example, no oil drops are shed by the interfacial waves along the cavity entrained by the steel sphere with $R_0 = 0.635\,\text{cm}$ (Fig. 13), one tiny oil drop is shed for the Teflon sphere with $R_0 = 0.953\,\text{cm}$ (indicated by the black arrow in Fig. 14), and many oil drops are shed for the largest Teflon sphere with $R_0 = 1.27\,\text{cm}$ (Fig. 7) (see the accompanying movies to these figures). As the size of the sphere radius approaches the oil lens radius, we expect that during entry the sphere produces greater shear at the three-phase (oil-water-air) contact line of the oil lens at the free surface. We also note that the Reynolds and Weber numbers at entry increase with sphere size, leading to an increase in inertial forces relative to viscous and surface tension forces, which may also produce greater shear.

Similarities exist between the perturbations formed along the cavity in our experiments and azimuthal harmonic disturbances to an air cavity generated by an azimuthally modified circular disk driven through water [24]; the oil-sphere-air contact line along the sphere and the disk form the lower boundaries to the air cavities in these two problems. In experiments, Enriquez *et al.* [24] show that the initial conditions imposed by the impacting disk, with an azimuthal disturbance of fixed mode and amplitude, has a lasting effect on the cavity structure, producing a highly regular

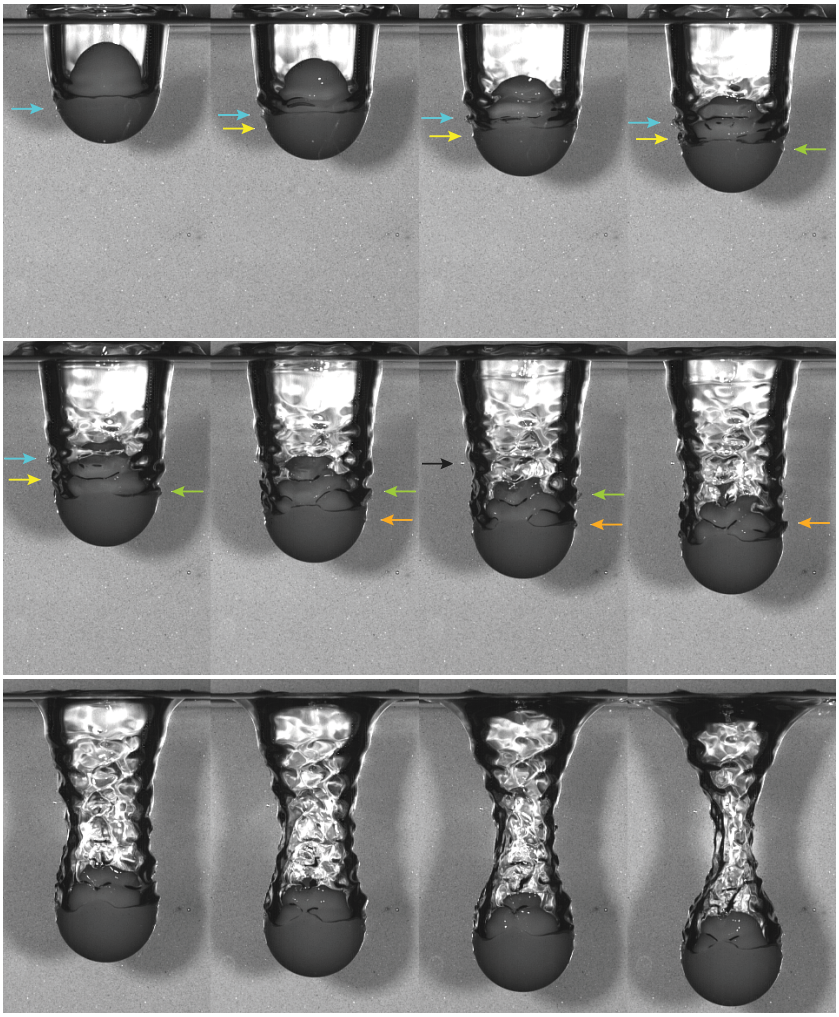

FIG. 14. Shear-induced perturbations that develop along the lower hemisphere of a 0.953-cm-radius Teflon sphere perturb the contact line which generates interfacial waves along the air cavity for the the oil lens experiment shown in Fig. 4(m). Times from impact are 22.9, 26.2, 29.6, 32.9, 36.2, 39.6, 42.9, 46.2, 52.9, 56.2, 59.6, 62.9 ms; the oil lens radius is 1.22 cm; and the experimental parameters are Bo = 17.5, Ca = 9.0×10^{-1}, Fr = 10.7, Re = 209, We = 187. Colored arrows track the evolution of a few individual disturbances and the black arrow is directed at an oil drop shed by the blue perturbation on the left-hand side of the cavity. Supplementary movie available online [28].

morphology resembling a "pineapple skin." In simulations, Enriquez *et al.* successfully capture the perturbed cavity shape and morphology by employing models for the axisymmetric cavity collapse [15] and the perturbation's amplitude [34]. Although the azimuthal disturbances to the contact line in our experiments are temporal and not of a fixed mode and amplitude, memory of these disturbances is retained as in Ref. [24], albeit in the form of an irregular morphology. Numerically modeling the perturbed surface in the oil lens experiments is more complicated than in the disk problem given the spatial irregularity and temporal nature of the perturbations to the contact line.

Cavity rupture, as shown in Fig. 7, occurs when the sphere radius is of equal or greater size than the lens radius. In this experiment, a defect develops along the front of the cavity wall that causes

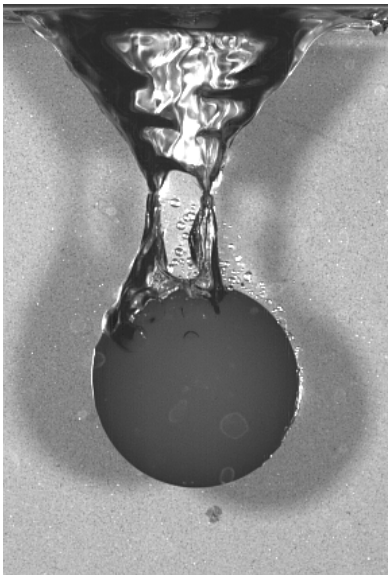

FIG. 15. Subcavities formed after initial rupture of the air cavity formed by a 1.27-cm-radius Delrin sphere in the oil lens experiment shown in Fig. 4(o) at 69.3 ms from impact with lens radius 1.30 cm, Bo = 31.2, Ca = 9.0×10^{-1}, Fr = 8.0, Re = 278, We = 249. Supplementary movie available online [28].

dewetting of the oil lining and a hole to form. As the hole grows larger, the cavity bifurcates into two separate subcavities with fluid occupying the region between the subcavities (indicated by the arrow in the first panel of Fig. 7). The subcavities next break up, leaving a trail of oil drops and small air bubbles in the wake of the receding upper and lower air cavities. Figure 15 provides another example of the hole and subcavities that form momentarily during cavity rupture.

In all of the oil lens experiments, a Worthington jet forms after cavity pinch-off or rupture. For smooth cavities in addition to a Worthington jet shooting upward, an opposite jet impinges upon the sphere apex inside the lower air cavity as shown in the second panel of Fig. 12. In all of the experiments, the oil that lines the upper cavity dewets as the upper cavity is directed upward by the Worthington jet [see the accompanying movies to Figs. 1(b), 7, 12, 14, and 15]. The leading edge of the oil film can remain azimuthally uniform or develop a fingering pattern as shown in Fig. 16. The compositions of the Worthington jet and the opposing jet, whether exclusively water or oil or a combination of the two, is not fully understood and worthy of further investigation.

We conjecture that the rippling structures along air-entraining cavities observed by Tan *et al.* [23] formed by oil-coated spheres entering water and by clean spheres entering a shallow layer of oil overlying water are produced by a similar shear-induced instability demonstrated in Figs. 13 and 14. We note that their two-layer experiments with steel spheres ($0.29 \leqslant D_0 \leqslant 1.43$ cm) conducted at impact speeds between 1.4 and 6 m s^{-1} have higher Froude numbers [$28 \leqslant \mathrm{Fr} \leqslant 2533$ with $\mathrm{Fr} = V_0^2/(gR_0)$] than in our study ($8 \leqslant \mathrm{Fr} \leqslant 43$), that their ratio of sphere diameter to oil layer thickness ($0.19 \leqslant D_0/h \leqslant 2.86$) is smaller than the ratio of our sphere diameter to oil lens thickness ($3.17 \leqslant D_0/h \leqslant 50.8$), and that the sunflower and silicone oils used for the upper layer in their study are 25% and over 24 times more viscous than oleic acid, respectively, which may account for differences exhibited by the perturbed cavities in our and Tan *et al.*'s study.

In one last point of comparison, Gekle *et al.* [19] and Mansoor *et al.* [22] find in experimental studies that smooth cavities can develop a kinked structure in the neck region prior to collapse. In a theoretical analysis, Gekle *et al.* [19] find that as the neck collapses, the air speed inside the neck increases substantially, leading to a large localized decrease in the pressure with suction

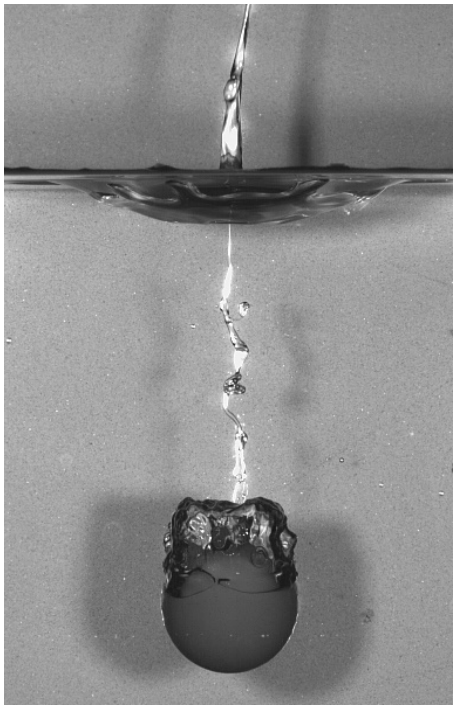

FIG. 16. The oil film that lines the air cavity wall before rupture in Fig. 4(m) dewets from the upper air cavity wall after rupture with the leading edge of the oil film, forming a fingering pattern as the cavity retracts to form a Worthington jet. Image is of a 0.953-cm-radius Teflon sphere 77.3 ms after impact with Bo = 17.5, Ca = 9.0×10^{-1}, Fr = 10.7, Re = 209, We = 187. See the supplementary movie [28] to Fig. 14.

strong enough to deform the cavity shape. In our experiments that develop perturbed cavities, the necked region of the cavities or subcavities have a highly angular, kinked form [e.g., see Figs. 4(m), 4(n), 7, and 15]. While there is some similarity in the structure of the neck with these studies, particularly at the length scale observed by Mansoor *et al.*, the kinks here are derived from the three-dimensional perturbations that form along the cavity when hydrostatic pressure forces the cavity to contract into an hourglass shape and which develop well before the singular events leading to pinch-off.

IV. CONCLUSIONS

We present a comparative experimental study on the low-speed vertical entry of spheres impacting onto water and onto a two-phase fluid, consisting of an oil lens floating on water, using spheres of different radii, densities, and materials.

Surface tension dominates in the water experiments where a quasistatic air cavity forms for smaller spheres and no cavity forms for larger spheres. All of the spheres are hydrophilic as water completely wets the spheres during entry.

Viscous effects dominate in the oil lens experiments providing the conditions for an air-entraining cavity to form with oil coating both the sphere front (rendering the sphere hydrophobic) and cavity wall. The cavities formed by all but the largest spheres pinch-off in deep seal closure while the cavities formed by the largest spheres rupture along the length of the cavity while tapering to an hourglass shape. Consistent with previous studies of hydrophobic spheres entering water, dimensionless values of the pinch-off time, pinch-off depth, and sphere depth at pinch-off decrease with decreasing density ratio, follow the predicted $\sqrt{\text{Fr}}$ scaling when sphere deceleration after

impact is negligible, and are nonlinearly related to $\sqrt{\mathrm{Fr}}$ when deceleration is non-negligible. We also find the pinch-off time follows the predicted $\sqrt{R_0/g}$ scaling for hydrophobic spheres.

Distinctive behavior observed in the oil lens experiments include the following:

(1) The sphere depth at pinch-off in all of the oil lens experiments collapses and scales logarithmically with the sphere mass independent of the density ratio or mode of breakup (deep seal closure or rupture).

(2) Cavities formed by spheres with high inertia develop a distinctive three-dimensional crumpled morphology before breakup that we demonstrate is due to a shear-induced instability. Specifically, perturbations that develop between the oil layer lining the sphere front and the surrounding water generate interfacial waves at the contact line that perturb the cavity wall. By contrast, cavities formed by spheres with low inertia remain smooth.

(3) As air evacuates the necked region during deep seal closure, an oil filament forms tethering the upper and lower air cavities together as they retract. The oil filament, which forms from the oil film lining the cavity wall, later breaks up into satellite drops.

For the low-speed impact conditions of this study, the presence of an oil lens less than 2 mm thick is critical to forming air-entraining cavities. Immiscible fluid layers are known to populate sea and ocean surfaces, such as oil slicks formed by spills or natural seepage that range in thickness from less than a micron to millimeters [35], and can be expected to influence entry by an impacting body as was recently found for the splash behavior of raindrops by Murphy *et al.* [35]. Our study highlights the effects that a thin immiscible lens on a water surface can have on the low-speed entry of an impacting sphere. Given the applications, high-speed entry is worthy of future examination as well.

ACKNOWLEDGMENTS

The authors thank Andrew Belmonte, Karen Daniels, Stephen Garoff, and Ann Juel for helpful discussions. We are grateful to Moises Veloz for his help in building the experimental apparatus. We acknowledge the support of the National Science Foundation Grant No. DMS-0707755.

[1] A. M. Worthington and R. S. Cole, Impact with a liquid surface, studied by the aid of instantaneous photography, Phil. Trans. R. Soc. London, Ser. A **189**, 137 (1897).

[2] A. M. Worthington and R. S. Cole, Impact with a liquid surface studied by the aid of instantaneous photography. Paper II, Phil. Trans. R. Soc. London, Ser. A **194**, 175 (1900).

[3] A. M. Worthington, *A Study of Splashes* (Longmans, Green and Company, London, 1908).

[4] A. Mallock, Sounds produced by drops falling on water, Proc. R. Soc. London, Ser. A **95**, 138 (1918).

[5] G. E. Bell, On the impact of a solid sphere with a fluid surface, Phil. Mag. J. Sci. **48**, 753 (1924).

[6] A. May, Effect of surface condition of a sphere on its water-entry cavity, J. Appl. Phys. **22**, 1219 (1951).

[7] G. Birkhoff and R. Isaacs, Transient cavities in air-water entry, Nav. Ordnance Rep. 1490, White Oak, MD, 1951.

[8] A. May, Vertical entry of missiles into water, J. Appl. Phys. **23**, 1362 (1952).

[9] J. W. Glasheen and T. A. McMahon, Vertical water entry of disks at low Froude numbers, Phys. Fluids **8**, 2078 (1996).

[10] M. Lee, R. G. Longoria, and D. E. Wilson, Cavity dynamics in high-speed water entry, Phys. Fluids **9**, 540 (1997).

[11] C. Duez, C. Ybert, C. Clanet, and L. Bocquet, Making a splash with water repellency, Nat. Phys. **3**, 180 (2007).

[12] V. Duclaux, F. Caillé, C. Duez, C. Ybert, L. Bocquet, and C. Clanet, Dynamics of transient cavities, J. Fluid Mech. **591**, 1 (2007).

[13] T. Grumstrup, J. B. Keller, and A. Belmonte, Cavity Ripples Observed during the Impact of Solid Objects into Liquids, Phys. Rev. Lett. **99**, 114502 (2007).
[14] J. M. Aristoff and J. W. M. Bush, Water entry of small hydrophobic spheres, J. Fluid Mech. **619**, 45 (2009).
[15] R. Bergmann, D. van der Meer, S. Gekle, A. van der Bos, and D. Lohse, Controlled impact of a disk on a water surface: Cavity dynamics, J. Fluid Mech. **633**, 381 (2009).
[16] M. Do-Quang and G. Amberg, The splash of a solid sphere impacting on a liquid surface: Numerical simulation of the influence of wetting, Phys. Fluids **21**, 022102 (2009).
[17] T. T. Truscott and A. H. Techet, Water entry of spinning spheres, J. Fluid Mech. **625**, 135 (2009).
[18] J. M. Aristoff, T. T. Truscott, A. H. Techet, and J. W. M. Bush, The water entry of decelerating spheres, Phys. Fluids **22**, 032102 (2010).
[19] S. Gekle, I. R. Peters, J. M. Gordillo, D. van der Meer, and D. Lohse, Supersonic Air Flow due to Solid-Liquid Impact, Phys. Rev. Lett. **104**, 024501 (2010).
[20] S. Gekle and J. M. Gordillo, Generation and breakup of Worthington jets after cavity collapse. Part 1. Jet formation, J. Fluid Mech. **663**, 293 (2010).
[21] J. O. Marston, I. U. Vakarelski, and S. T. Thoroddsen, Cavity formation by the impact of Leidenfrost spheres, J. Fluid Mech. **699**, 465 (2012).
[22] M. M. Mansoor, J. O. Marston, I. U. Vakarelski, and S. T. Thoroddsen, Water entry without surface seal: Extended cavity formation, J. Fluid Mech. **743**, 295 (2014).
[23] B. C.-W. Tan, J. H. A. Vlaskamp, P. Denissenko, and P. J. Thomas, Cavity formation in the wake of falling spheres submerging into a stratified two-layer system of immiscible liquids, J. Fluid Mech. **790**, 33 (2016).
[24] O. R. Enriquez, I. R. Peters, S. Gekle, L. E. Schmidt, D. Lohse, and D. van der Meer, Collapse and pinch-off of a non-axisymmetric impact-created air cavity in water, J. Fluid Mech. **701**, 40 (2012).
[25] T. T. Truscott, B. P. Epps, and J. Belden, Water entry of projectiles, Annu. Rev. Fluid Mech. **46**, 355 (2014).
[26] J. W. Glasheen and T. A. McMahon, A hydrodynamic model of locomotion in the basilisk lizard, Nature (London) **380**, 340 (1996).
[27] L. B. Smolka, C. K. McLaughlin, and T. P. Witelski, Oil capture from a water surface by a falling sphere, Colloids Surf. A **497**, 126 (2016).
[28] See Supplemental Material at http://link.aps.org/supplemental/10.1103/PhysRevFluids.4.044001 for supplementary movies.
[29] M. Manga and H. A. Stone, Low Reynolds number motion of bubbles, drops, and rigid spheres through fluid-fluid interfaces, J. Fluid Mech. **287**, 279 (1995).
[30] J.-L. Pierson and J. Magnaudet, Inertial settling of a sphere through an interface. Part 1. From sphere flotation to wake fragmentation, J. Fluid Mech. **835**, 762 (2018).
[31] A. W. Adamson and A. P. Gast, *Physical Chemistry of Surfaces*, 6th ed. (Wiley-Interscience, New York, 1997).
[32] D. W. Camp and J. C. Berg, The spreading of oil on water in the surface-tension regime, J. Fluid Mech. **184**, 445 (1987).
[33] H. A. Stone, B. J. Bentley, and L. G. Leal, An experimental study of transient effects in the breakup of viscous drops, J. Fluid Mech. **173**, 131 (1986).
[34] L. E. Schmidt, N. C. Keim, W. W. Zhang, and S. R. Nagel, Memory-encoding vibrations in a disconnecting air bubble, Nat. Phys. **5**, 343 (2009).
[35] D. W. Murphy, C. Li, V. d'Albignac, D. Morra, and J. Katz, Splash behaviour and oily marine aerosol production by raindrops impacting oil slicks, J. Fluid Mech. **780**, 536 (2015).